

Scalar-Field Wave Dynamics and Quasinormal Modes of the Teo Rotating Wormhole

Ramesh Radhakrishnan* and Gerald B. Cleaver†

*Department of Physics, Baylor University, Waco, Texas 76798, USA and
Early Universe, Cosmology and Strings (EUCOS) Group, Center for Astrophysics,
Space Physics and Engineering Research (CASPER), Baylor University, Waco, Texas 76798, USA*

Delaram Mirfendereski‡

*Department of Physics and Astronomy, The University of Texas Rio Grande Valley, USA and
Early Universe, Cosmology and Strings (EUCOS) Group, Center for Astrophysics,
Space Physics and Engineering Research (CASPER), Baylor University, Waco, Texas 76798, USA*

Eric W. Davis§

*Department of Physics, State University of New York at Albany, Albany, New York 12222, USA and
Early Universe, Cosmology and Strings (EUCOS) Group, Center for Astrophysics,
Space Physics and Engineering Research (CASPER), Baylor University, Waco, Texas 76798, USA*

Claudio Cremaschini¶

*Institute of Physics and Research Center for Theoretical Physics and Astrophysics,
Faculty of Philosophy and Science, Silesian University in Opava,
Bezručovo nám. 13, CZ-74601 Opava, Czech Republic*

(Dated: December 30, 2025)

We analyze scalar-field perturbations of the rotating Teo wormhole and compute its quasinormal-mode (QNM) spectrum using WKB methods in a fully horizonless geometry. The Klein–Gordon equation separates and yields a Schrödinger-type radial equation with a single, smooth potential barrier shaped by the localized frame-dragging profile of the wormhole throat. This barrier supports damped oscillatory modes across the full spin range examined.

The resulting QNM spectrum exhibits a coherent and monotonic dependence on rotation. As the spin increases, both the oscillation frequency $\text{Re}(\omega)$ and the damping rate $-\text{Im}(\omega)$ decrease, indicating progressively longer-lived modes in the absence of horizon-induced absorption. In the eikonal limit, we extract the photon-ring radius, orbital frequency, and Lyapunov exponent, and verify the standard correspondence $\omega_{\text{QNM}} \simeq m \Omega_{\text{ph}} - i(n + \frac{1}{2})\lambda$.

Comparison with Kerr black holes reveals qualitative differences. Whereas Kerr QNMs are governed by horizon absorption and exhibit symmetric prograde/retrograde mode splitting, the Teo wormhole displays a stronger but spatially confined spin response, partial reflection at the throat, and a distinctive one-sided $m = \pm 2$ splitting that saturates rapidly with increasing spin. Although the rotating Teo wormhole admits an ergoregion and superradiant-compatible frequency kinematics, the absence of an event horizon or dissipative boundary prevents classical superradiant amplification. These results demonstrate how rotation and boundary conditions jointly shape wave propagation in horizonless compact objects and provide characteristic spectral signatures distinguishing rotating wormholes from Kerr black holes.

Contents

I. Introduction	3	A. Photon Rings and Stability Analysis	5
II. Teo Wormhole Geometry and Perturbation Setup	4	B. On the Unstable Nature of the Photon Ring	6
A. Klein–Gordon equation for the Teo wormhole	4	C. Connection to Quasinormal Modes	6
III. Effective Potential and Circular Photon Orbits	5	D. Variation of the Klein–Gordon Effective Potential with the Rotation Parameter	6
		E. Effective potential and photon ring	7
		F. Photon-ring properties	7
		G. Eikonal QNM–photon–ring correspondence	8
		IV. Quasinormal Modes and WKB Approximation	8
		A. WKB Approximation and Strategy	8
		B. Remarks on applicability of the WKB method	8
		C. Quasinormal Modes and First-Order WKB Estimate	9

* ramesh_radhakrishna1@baylor.edu

† gerald_cleaver@baylor.edu

‡ delaram.mirfendereski@utrgv.edu

§ ewdavis@albany.edu

¶ claudio.cremaschini@physics.slu.cz

D. Effective potential and WKB estimate	9
E. Effective potential and WKB peaks for different azimuthal numbers	9
F. Quasinormal Mode Dependence on Spin Parameter	10
G. Overtone dependence of quasinormal modes	10
V. Geometric and Physical Phenomena	11
A. Mode-Splitting in the Rotating Teo Wormhole	11
B. Ergoregion and Its Geometric Role	12
C. Superradiant Kinematics and Its Connection to Mode-Splitting	12
D. Ergoregion and Superradiant-Compatible Domain	13
E. Physical Interpretation	13
VI. Comparison with Kerr Rotating Black Hole	14
A. Baseline Comparison: Boundary Conditions and Frequency Trends	14
B. Mode-Splitting and Frame-Dragging Asymmetry	14
C. Damping-Rate Splitting and Zero-Damped Modes	15
VII. Numerical Methods	15
VIII. Possible physical interpretation of the scalar field Φ	16
IX. Conclusions and Future Outlook	16
A. Generation of Mock Kerr and Teo Data	17
1. Conceptual construction of the mock datasets	17
2. Python code used to generate the datasets	18
B. Extended Comparison Between Teo and Kerr	18
References	20

I. Introduction

Rotating traversable wormholes provide a natural extension of static Morris–Thorne geometries by including angular momentum, an ingredient ubiquitous in astrophysical environments. The Teo rotating wormhole metric [1] is a particularly useful toy model which extends the Morris–Thorne construction to a stationary, axially symmetric, traversable geometry. It admits a smooth throat without horizons, while its rotation parameter introduces frame dragging, mode splitting, and superradiant-compatible kinematic regimes. Because most compact astrophysical objects from stars and planets to galaxies exhibit rotation, the study of rotating wormholes is both physically and observationally motivated. In [1], Teo also noted the possible presence of an ergoregion surrounding the throat. The defining feature of the ergoregion is frame dragging.

As with static traversable wormholes, the stress-energy tensor required to sustain Teo’s metric necessarily violates the Null Energy Condition (NEC) in at least some region near the throat (e.g. $T_{\hat{t}\hat{t}} + T_{\hat{r}\hat{r}} < 0$). Crucially, however, rotation partially localizes this exoticity: the NEC violation can be confined to limited regions rather than being uniformly distributed around the throat, and the spatial distribution of negative-energy regions depends on the choice of rotation profile. Teo explicitly showed that, for suitable model parameters, there exist classes of null and timelike geodesics that traverse the wormhole without ever entering the NEC-violating zones [1]. This feature echoes earlier observations by Visser that one can construct wormhole geometries in which a traveller follows a geodesic that avoids regions of exotic matter [2], and subsequent work has quantified how the total amount of energy-condition violation can be made arbitrarily small in carefully engineered geometries [3]. Thus, while exotic matter is unavoidable for global traversability, rotation permits a partial redistribution of exoticity and allows certain trajectories to experience an effectively “normal” spacetime. The Teo metric therefore offers a simple but realistic laboratory for understanding wave propagation and stability in rotating wormhole backgrounds.

Recent gravitational-wave detections by LIGO–Virgo–KAGRA have opened an unprecedented window into the strong-gravity regime [4–6]. The classic ringdown signal, observed during mergers of massive compact objects such as black holes or neutron stars, corresponds to the exponentially damped oscillations of the remnant as it settles into a stable configuration. While the observed ringdown spectra are consistent with the predictions of general-relativistic black holes, there remains interest in exploring whether exotic compact objects (ECOs), such as wormholes, could mimic these signals [7–9]. Searches for late-time “echoes”, which are secondary bursts of gravitational waves arising from partial reflections of the initial ringdown signal within the compact object’s interior or near-horizon structure, or deviations from the

Kerr ringdown have so far yielded inconclusive or statistically marginal results [10, 11]. This observational uncertainty motivates continued theoretical modeling of wave scattering in alternative compact objects to provide discriminants for future searches. In particular, a clear understanding of the quasinormal-mode (QNM) spectrum of wormholes is essential for predicting the characteristic frequencies, damping times, and potential echo delays that would distinguish them from black holes.

QNMs are complex oscillation frequencies that usually appear in the response of a black-hole spacetime to initial perturbations [12, 13]. The study of QNMs is of great significance in the field of gravitational-wave research [14, 15]. QNMs carry information on the reaction of spacetime and various properties of black holes such as mass, charge, and angular momentum through their characteristic waveform [16, 17]. The imaginary part of QNMs is related to the damping time scale. This can be used to investigate the stability of the Teo wormhole [18, 19]. It is hard to find an exact analytical solution for the QNM eigenfrequencies. Several approximation methods have been used in the past, including the WKB approximation [20]. Higher-order corrections to WKB were also used by other authors [21, 22]. A study similar to this paper has been done for spherically symmetric compact objects [23].

In this paper, we analyze scalar-field dynamical interaction in the form of perturbations on the axisymmetric Teo rotating wormhole background as a tractable first step toward a full tensorial perturbation study. A minimally coupled scalar field serves as a test probe that captures the essential physics of wave propagation and potential barriers in curved spacetimes, while avoiding the technical complications of metric perturbations [24, 25]. By studying the Klein–Gordon equation on the Teo geometry, we derive an effective potential $V_{\text{eff}}(r)$ governing the radial propagation of scalar waves. The multipole number ℓ nominally labels the angular structure of scalar perturbations and enters the effective potential as a parameter controlling the barrier height, while the azimuthal number m couples to the wormhole rotation and introduces a frame-dragging dependence in V_{eff} . In our current calculations, we primarily explore representative m -values. While the effective potential includes the rotational m -dependence, and we observe mode splitting, the full pattern of m -splitting across all azimuthal numbers is not systematically resolved.

We perform an exploratory computation of the associated QNMs using a first-order Wentzel–Kramers–Brillouin (WKB) approximation [20, 26, 27], which relies on the peak of $V_{\text{eff}}(r)$ and its derivatives. The analysis of V_{eff} provides direct insight into the scattering properties of the wormhole throat, including possible single- or double-peak features that can give rise to long-lived modes, also referred to as trapped modes or quasi-bound states. These correspond to oscillations that decay very slowly due to partial confinement of the scalar field between potential barriers or wells [28–30]. Such long-lived

modes are characterized by a small imaginary part of the QNM frequency, reflecting their slow damping, and in some parameter regimes they may produce late-time echoes in the waveform, though echoes are not guaranteed.

Our goal is to map the qualitative dependence of the fundamental QNM frequencies on the wormhole rotation parameter (a), throat size ($r = b_0$), azimuthal number (m), and overtone number (n), while clearly delineating the parameter regimes where the first-order WKB approximation provides reliable predictions and noting that m -splitting, ergoregion formation, superradiant-compatible kinematics, and other rotational effects may also be observed.

II. Teo Wormhole Geometry and Perturbation Setup

A. Klein–Gordon equation for the Teo wormhole

We begin with the Klein–Gordon (KG) equation for a massless scalar field

$$\square\Phi = \frac{1}{\sqrt{-g}} \partial_\mu \left(\sqrt{-g} g^{\mu\nu} \partial_\nu \Phi \right) = 0, \quad (1)$$

propagating on the rotating Teo wormhole geometry. Throughout this work we adopt the equatorial-plane specialization of the Teo metric, which retains all rotational effects while simplifying the algebraic structure of the KG operator.

Metric functions and equatorial-plane reduction

The full Teo line element is

$$ds^2 = -N^2(r, \theta) dt^2 + \frac{dr^2}{1 - b_0/r^2} + r^2 K^2(r, \theta) d\theta^2 + r^2 K^2(r, \theta) \sin^2 \theta (d\phi - \Omega(r) dt)^2, \quad (2)$$

where

$$\Omega(r) = 2a/r^3 \quad (3)$$

generates frame dragging. For analytic tractability and because the qualitative rotational physics is unaffected, we evaluate the metric at $\theta = \pi/2$ with $N(r, \theta) = K(r, \theta) = 1$. For equatorial trajectories, we further restrict to $d\theta = 0$.

The nonvanishing metric components then reduce to

$$g_{tt} = -1 + r^2 \Omega^2(r), \quad (4)$$

$$g_{t\phi} = -r^2 \Omega(r), \quad (5)$$

$$g_{\phi\phi} = r^2, \quad (6)$$

$$g_{rr} = \left(1 - \frac{b_0}{r^2}\right)^{-1}, \quad (7)$$

$$g_{\theta\theta} = r^2, \quad (8)$$

with inverse components

$$g^{tt} = -1, \quad g^{t\phi} = -\Omega(r), \quad g^{\phi\phi} = \frac{1 - r^2 \Omega^2(r)}{r^2}, \quad (9)$$

$$g^{rr} = 1 - \frac{b_0}{r^2}, \quad g^{\theta\theta} = \frac{1}{r^2}. \quad (10)$$

The determinant simplifies to

$$\sqrt{-g} = r^2 \left(1 - \frac{b_0}{r^2}\right)^{-1/2}. \quad (11)$$

Mode decomposition

Stationarity and axial symmetry allow the decomposition

$$\Phi(t, r, \theta, \phi) = e^{-i\omega t} e^{im\phi} \Psi(r, \theta), \quad (12)$$

so that the time–angular sector of the KG operator becomes

$$\omega^2 g^{tt} - 2m\omega g^{t\phi} + m^2 g^{\phi\phi} = -(\omega - m\Omega(r))^2 + \frac{m^2}{r^2}. \quad (13)$$

We are interested in scalar configurations that remain confined to the equatorial plane, $\partial_\theta \Phi = 0$, so that all θ -derivatives in (1) drop out. The KG equation then takes the form

$$\left[-(\omega - m\Omega)^2 + \frac{m^2}{r^2}\right] \Phi + \frac{1}{\sqrt{-g}} \partial_r \left(\sqrt{-g} g^{rr} \Phi' \right) = 0. \quad (14)$$

Radial operator and tortoise coordinate

Using the explicit form of $\sqrt{-g} g^{rr}$,

$$\sqrt{-g} g^{rr} = r^2 \sqrt{1 - \frac{b_0}{r^2}},$$

the radial operator becomes

$$\frac{1}{\sqrt{-g}} \partial_r \left(\sqrt{-g} g^{rr} \Phi' \right) = \frac{\sqrt{1 - b_0/r^2}}{r^2} \frac{d}{dr} \left(r^2 \sqrt{1 - \frac{b_0}{r^2}} \Phi' \right). \quad (15)$$

It is convenient to introduce the tortoise coordinate

$$\frac{dr_*}{dr} = \frac{1}{\sqrt{1 - b_0/r^2}}, \quad (16)$$

which regularizes the throat at $r^2 = b_0$. In terms of r_* , the radial operator becomes

$$\frac{d^2 \Phi}{dr_*^2} + P(r) \frac{d\Phi}{dr_*}, \quad P(r) = \frac{2}{r} \sqrt{1 - \frac{b_0}{r^2}}. \quad (17)$$

Thus, even in the tortoise coordinate a first-derivative term remains, so an additional field redefinition is required before a Schrödinger-type equation can emerge.

Liouville transformation and Schrödinger form

To eliminate the first-derivative term we introduce the standard Liouville transformation

$$\Phi(r_*) = A(r) \Psi(r_*), \quad \frac{A'}{A} = -\frac{P}{2}, \quad (18)$$

where a prime denotes differentiation with respect to r_* . Substituting (18) into (14) yields the Schrödinger-type master equation

$$\frac{d^2\Psi}{dr_*^2} + \left[\omega^2 - V_{\text{eff}}(r) \right] \Psi = 0. \quad (19)$$

The effective potential is

$$V_{\text{eff}}(r) = (\omega - m\Omega)^2 - \frac{m^2}{r^2} + \frac{P'}{2} + \frac{P^2}{4}, \quad (20)$$

where $P(r)$ is given by (17). The last two terms encode the geometric contributions arising from the radial measure and are essential for placing the KG equation into Sturm–Liouville form. These terms must be retained (even when small) for any WKB analysis based on the Schrödinger-type equation (19).

Relation to the co-rotating KG potential

If one temporarily omits the geometric corrections $P'/2$ and $P^2/4$ —as is appropriate only in the geometric-optics limit—the potential reduces to the algebraic Klein–Gordon form

$$V_{\text{eff}}(r) = (\omega - m\Omega)^2 - \frac{m^2}{r^2}, \quad (21)$$

which is the expression used for photon-ring analysis and for establishing the geometric correspondence between quasinormal modes and unstable circular null orbits. In the eikonal (geometric-optics) limit, we therefore identify this quantity as the effective potential $V_{\text{eff}}^{(\text{eikonal})}$. In contrast, the Schrödinger potential (20) must be used for WKB quasinormal-mode calculations.

III. Effective Potential and Circular Photon Orbits

For null geodesics confined to the equatorial plane of the rotating Teo wormhole spacetime, an effective radial potential governs the motion of photons and the formation of photon rings. The frame-dragging angular velocity is given by (3).

From the Klein–Gordon reduction in the equatorial plane, the radial part of the separated wave equation naturally suggests an *eikonal* effective potential of the form

$$V_{\text{eff}}(r) = (\omega - m\Omega(r))^2 - \frac{m^2}{r^2}, \quad (22)$$

where ω and m label the Fourier mode of the scalar field. For the canonical Teo wormhole with $\Omega(r) = 2a/r^3$, this becomes

$$V_{\text{eff}}(r) = -\frac{m^2}{r^2} + \frac{(\omega r^3 - 2am)^2}{r^6}, \quad (23)$$

whose first derivative is

$$V'_{\text{eff}}(r) = \frac{12am\omega}{r^4} - \frac{24a^2m^2}{r^7} + \frac{2m^2}{r^3}, \quad (24)$$

and the second derivative, governing local stability, is

$$V''_{\text{eff}}(r) = -\frac{48am\omega}{r^5} + \frac{168a^2m^2}{r^8} - \frac{6m^2}{r^4}. \quad (25)$$

The sign of $V''_{\text{eff}}(r)$ at an extremum distinguishes unstable ($V'' < 0$) from stable ($V'' > 0$) circular configurations in the eikonal wave picture.

Here, ω denotes the wave-mode frequency associated with the temporal oscillation of the perturbation, while $\Omega(r)$ represents the frame-dragging angular velocity of the rotating wormhole geometry. In the geometric-optics (high-frequency) limit, the dispersion relation implied by (22) coincides with the Hamilton–Jacobi equation for null geodesics, so the same radial structure governs both the eikonal KG modes and the photon trajectories.

A. Photon Rings and Stability Analysis

In the context of the Teo rotating wormhole [1], photon rings correspond to unstable circular null geodesics that form the boundary of the observable shadow or bright emission ring seen by distant observers [31]. These orbits occur at the radius $r = r_{\text{ph}}$ where photons can temporarily orbit the wormhole throat under the balance of centrifugal repulsion and frame-dragging effects.

In this work we treat the photon ring in two complementary ways. On the one hand, we obtain $r_{\text{ph}}(a, b)$ from the *null geodesic equations* by solving the circular-orbit conditions $F(r, b) = 0$ and $\partial_r F(r, b) = 0$, where $b = L/E$ is the impact parameter. Here $F(r, b)$ denotes the radial null-geodesic potential obtained from the Hamiltonian constraint $g^{\mu\nu} p_\mu p_\nu = 0$, with conserved energy $E \equiv -p_t$ and angular momentum $L \equiv p_\phi$ arising from stationarity and axial symmetry, respectively. Circular photon orbits correspond to extrema of $F(r, b)$.

On the other hand, the eikonal Klein–Gordon potential (22) provides a convenient wave-based proxy: in the geometric-optics limit, the phase $\Phi \sim e^{iS/\hbar}$ obeys the Hamilton–Jacobi equation $g^{\mu\nu} \partial_\mu S \partial_\nu S = 0$, which is equivalent to the null geodesic condition [14, 28]. Consequently, the extrema of $V_{\text{eff}}(r)$ track the circular null orbits, and its curvature at the peak encodes the same instability information as the Lyapunov exponent computed from geodesic deviation [14, 28, 32].

The photon ring radius is determined by the geodesic conditions

$$F(r_{\text{ph}}, b) = 0, \quad \partial_r F(r, b)|_{r=r_{\text{ph}}} = 0, \quad (26)$$

which identify an unstable circular null orbit. In the eikonal picture, one may equivalently locate a nearby radius by solving

$$\left. \frac{dV_{\text{eff}}}{dr} \right|_{r=r_{\text{peak}}} = 0, \quad \left. \frac{d^2V_{\text{eff}}}{dr^2} \right|_{r=r_{\text{peak}}} < 0, \quad (27)$$

for fixed (ω, m) , with r_{peak} lying close to r_{ph} in the high-frequency limit.

The quantity $\Omega_{\text{ph}} = (d\phi/dt)_{r_{\text{ph}}}$ represents the orbital frequency of photons at the unstable circular orbit, corresponding to the frame-dragging rate measured by a distant observer. In the eikonal regime, this frequency is related to the real part of the quasinormal frequency via

$$\omega_R/m \simeq \Omega_{\text{ph}},$$

providing a direct bridge between photon-ring properties and the wave spectrum.

To quantify the orbit's instability, we compute the Lyapunov exponent λ [28]:

$$\lambda = \sqrt{-\frac{V''_{\text{geo}}(r_{\text{ph}})}{2\dot{t}^2}}, \quad (28)$$

where $V_{\text{geo}}(r)$ denotes the *geodesic* radial potential and $\dot{t} = dt/d\tau$ is obtained from the first integrals. For equatorial null motion in the Teo metric,

$$ds^2 = -N^2(r) dt^2 + \frac{dr^2}{1 - b_0/r^2} + r^2[d\phi - \Omega(r) dt]^2, \quad (29)$$

the conserved quantities

$$E = -g_{tt}\dot{t} - g_{t\phi}\dot{\phi}, \quad L = g_{t\phi}\dot{t} + g_{\phi\phi}\dot{\phi}$$

lead to

$$\dot{t} = \frac{Eg_{\phi\phi} + Lg_{t\phi}}{g_{t\phi}^2 - g_{tt}g_{\phi\phi}}. \quad (30)$$

At the circular photon orbit this simplifies to

$$\dot{t} = \frac{E}{N^2(r)}, \quad (31)$$

so that

$$\lambda_t = \frac{N^2(r_{\text{ph}})}{E} \sqrt{-\frac{V''_{\text{geo}}(r_{\text{ph}})}{2}}. \quad (32)$$

Here the subscript t indicates that the Lyapunov exponent is defined with respect to the coordinate time t measured by a distant observer, rather than the affine parameter along the null geodesic. With the standard normalization $E = 1$ and $N = 1$ for the Teo wormhole,

$$\lambda_t = \sqrt{-\frac{V''_{\text{geo}}(r_{\text{ph}})}{2}}. \quad (33)$$

In the eikonal limit the curvature of V_{geo} at r_{ph} coincides with that of the KG-derived potential V_{eff} to leading order, so one may interchange them for practical computations of λ .

A larger λ indicates stronger local instability of the orbit. These quantities are plotted in Fig. 3. The photon ring consistently lies outside the ergosurface radius $r_{\text{ergo}} = \sqrt{2a}$, mirroring the geometric ordering in Kerr.

B. On the Unstable Nature of the Photon Ring

The photon ring in the rotating Teo wormhole arises from the *unstable* branch of the effective potential, characterized by $V''_{\text{geo}}(r_{\text{ph}}) < 0$. At this location, photons occupy circular null geodesics at the crest of the potential barrier: even infinitesimal radial perturbations cause them to escape outward or fall inward toward the throat. This instability defines the sharp optical edge of the photon ring in ray-tracing simulations [31]. The Lyapunov exponent λ quantifies the divergence of nearby photon trajectories and directly determines the imaginary part of the corresponding quasinormal modes [28]. This mirrors the situation in black holes such as Kerr [33]. Thus, the unstable branch of the radial potential encodes both optical and perturbative signatures of the Teo wormhole spacetime.

C. Connection to Quasinormal Modes

In the eikonal limit, where the perturbation wavelength is much smaller than the curvature radius, the dynamics of wave propagation is governed by the same barrier that controls the unstable circular null orbits. Consequently, the photon-ring parameters $(r_{\text{ph}}, \Omega_{\text{ph}}, \lambda)$ extracted from the null geodesics (or equivalently from V_{eff} in the geometric-optics limit) encode the leading-order behavior of quasinormal modes [14, 28, 34]. The real and imaginary parts of the QNM frequency follow

$$\omega_{\text{QNM}} \simeq m\Omega_{\text{ph}} - i\left(n + \frac{1}{2}\right)\lambda. \quad (34)$$

This correspondence unifies geometric optics and wave dynamics in the Teo wormhole spacetime and provides a useful benchmark for the full WKB analysis based on the Schrödinger-form potential.

D. Variation of the Klein–Gordon Effective Potential with the Rotation Parameter

Figure 1 shows the Klein–Gordon effective potential

$$V_{\text{eff}}(r) = (\omega - m\Omega(r))^2 - \frac{m^2}{r^2}, \quad \Omega(r) = \frac{2a}{r^3}, \quad (35)$$

evaluated for several values of the rotation parameter a . This potential arises directly from the separated scalar-wave equation and captures how frame dragging modifies the propagation of high-frequency scalar perturbations in the Teo wormhole spacetime. It is distinct from the Schrödinger-form potential used later for the WKB analysis and does not form a trapping barrier near the throat.

As the rotation parameter increases, the term $m\Omega(r)$ grows rapidly at small radii, producing the steep inner

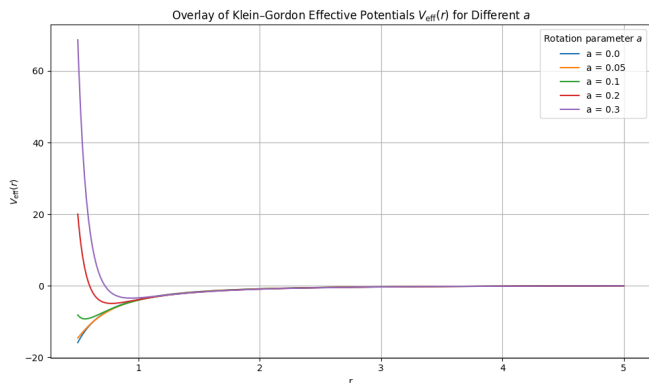


FIG. 1. Klein–Gordon effective potential $V_{\text{eff}}(r)$ for several rotation parameters a . Larger a increases the magnitude of the near-throat contribution $m\Omega(r) \propto a/r^3$, producing a steeper rise in the inner region. At large radii, frame dragging becomes negligible and all curves approach the asymptotic value $V_{\text{eff}} \rightarrow \omega^2$. This potential is derived from the separated scalar wave equation and is distinct from the Schrödinger-form potential used in the WKB analysis.

rise in the potential. At larger radii the frame-dragging term decays as r^{-3} , so all curves approach the asymptotic limit $V_{\text{eff}}(r) \rightarrow \omega^2$, reflecting the asymptotic flatness of the geometry on both sides.

Because this Klein–Gordon potential does not develop a barrier, it is not used to determine photon-ring radii or quasinormal-mode peaks. Its role here is purely illustrative: it shows how rotation reshapes the co-rotating wave potential that appears in the Hamilton–Jacobi/eikonal correspondence, while the actual photon-ring properties and WKB peaks are computed later from geodesics and from the Schrödinger-form potential.

E. Effective potential and photon ring

Figure 2 displays the Klein–Gordon (KG) effective potential $V_{\text{eff}}^{(\text{KG})}(r)$ evaluated on the equatorial plane of the rotating Teo wormhole for a representative spin value. This potential arises from the separated scalar wave equation; it is therefore a wave-propagation potential and does *not* determine the location of the null circular geodesics. Its purpose here is to illustrate how scalar perturbations perceive the near-throat geometry, and to provide a qualitative comparison with the photon ring obtained independently from the geodesic equations.

The vertical red dashed line marks the photon-ring radius r_{ph} computed from the null circular geodesic conditions $F(r, b) = 0$ and $\partial_r F(r, b) = 0$. Although the Klein–Gordon effective potential arises from the separated scalar wave equation and does not, in principle, determine the location of null circular geodesics, its extremum is found to lie very close to r_{ph} for the representative parameters shown here. This near-coincidence reflects the familiar eikonal correspondence between wave dynamics and unstable null orbits, while the two quantities remain conceptually distinct and are obtained from independent equations.

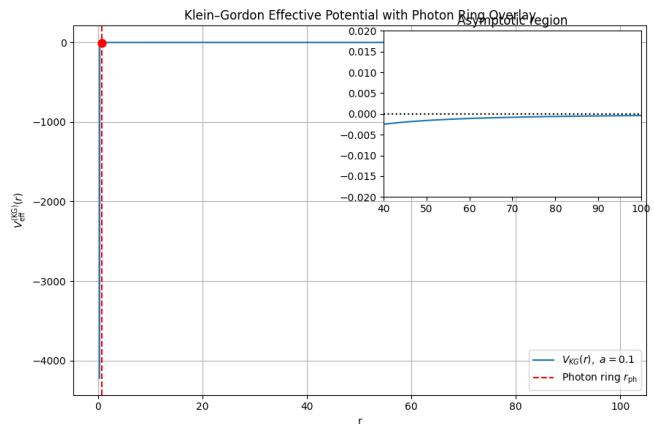


FIG. 2. Klein–Gordon effective potential $V_{\text{eff}}^{(\text{KG})}(r)$ for the rotating Teo wormhole, extended to $r = 100$ to verify the correct asymptotic decay. The inset shows a zoom of the far-region behavior where $V_{\text{eff}}^{(\text{KG})}(r) \rightarrow 0^-$. The vertical dashed red line marks the photon-ring radius r_{ph} obtained independently from the null circular-geodesic conditions. Although the KG potential does not determine r_{ph} , its extremum lies close to the photon ring for the representative parameters shown here, reflecting the familiar eikonal correspondence between wave dynamics and unstable null orbits.

To demonstrate the correct asymptotic behavior, the radial domain is extended to $r = 100$. The inset shows a magnified view of the large- r region, confirming that $V_{\text{eff}}^{(\text{KG})}(r)$ approaches zero smoothly from below, $V_{\text{eff}}^{(\text{KG})}(r) \rightarrow 0^-$, in accordance with the asymptotic flatness of the Teo wormhole spacetime.

F. Photon-ring properties

The photon-ring radius r_{ph} , the corresponding angular frequency $|\Omega_{\text{ph}}|$, and the Lyapunov exponent λ are obtained entirely from the null circular-geodesic conditions,

$$F(r, b) = 0, \quad \partial_r F(r, b) = 0,$$

where $F(r, b)$ is constructed from the inverse metric components $g^{tt}, g^{t\phi}, g^{\phi\phi}$ of the Teo wormhole. No Klein–Gordon (KG) approximations enter these quantities; they follow directly from the geodesic structure of the spacetime.

Figure 3 shows the dependence of the three photon-ring parameters on the rotation parameter a . Several robust trends emerge. First, the radius r_{ph} increases monotonically with a , indicating that frame dragging pushes the unstable circular null orbit outward from the throat. Second, the orbital frequency $|\Omega_{\text{ph}}|$ decreases as a grows, because the outward shift in r_{ph} dominates over the increase in the local frame-dragging rate. Finally, the Lyapunov exponent λ also decreases with increasing a , signalling that the photon ring becomes less unstable at higher rotation, consistent with the broadening of the near-throat potential barrier seen in geodesic analyses.

These behaviors collectively imply that a rapidly rotating Teo wormhole produces a larger, slower, and more

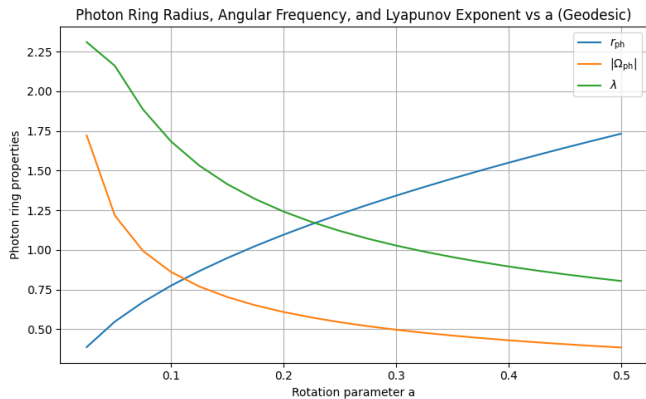


FIG. 3. Photon-ring radius r_{ph} , angular frequency $|\Omega_{\text{ph}}|$, and Lyapunov exponent λ as functions of the rotation parameter a , computed entirely from the null circular-geodesic conditions. Increasing a shifts the photon ring outward, lowers the orbital frequency, and reduces the instability of the orbit.

weakly unstable photon ring—properties that leave distinct signatures in its optical appearance and quasinormal-mode spectrum.

G. Eikonal QNM–photon–ring correspondence

In the eikonal (geometric-optics) limit, the real and imaginary parts of the quasinormal frequencies are determined directly by the photon ring via

$$\omega_R \simeq m |\Omega_{\text{ph}}|, \quad -\omega_I \simeq \left(n + \frac{1}{2}\right) \lambda,$$

where m is the azimuthal number and n the overtone index. Since both $|\Omega_{\text{ph}}|$ and λ decrease monotonically with a , the eikonal QNM frequencies inherit the same trend: the oscillation frequency drops, and the damping rate weakens as the wormhole rotates faster.

Figure 4 displays these two relations for $m = 2$ and $n = 0$. The good agreement between the geometric quantities and the eikonal QNM predictions confirms the internal consistency of the geodesic and wave pictures for the Teo wormhole.

IV. Quasinormal Modes and WKB Approximation

A. WKB Approximation and Strategy

After separation of variables in the Teo metric and restriction to the equatorial-plane background, the massless Klein-Gordon equation reduces, under the approximations described in Sec. II A, to a Schrödinger-type wave equation

$$\frac{d^2 \Psi}{dr_*^2} + \left[\omega^2 - V_{\text{eff}}^{(\text{Schr})}(r) \right] \Psi = 0, \quad (36)$$

where r_* is the tortoise coordinate defined by $dr_*/dr = (1 - b_0/r^2)^{-1/2}$, and $V_{\text{eff}}^{(\text{Schr})}(r)$ is the *Schrödinger-form*

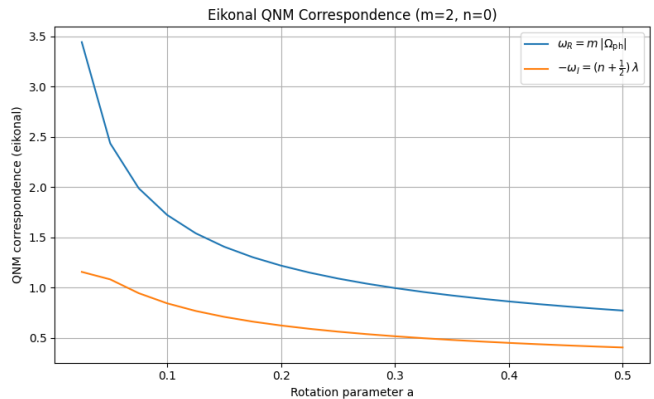


FIG. 4. Eikonal QNM correspondence for the Teo wormhole. The real part $\omega_R \simeq m |\Omega_{\text{ph}}|$ (blue) and the damping rate $-\omega_I \simeq (n + \frac{1}{2}) \lambda$ (orange) both decrease as the rotation parameter a increases, reflecting the outward shift and reduced instability of the photon ring.

potential. Using the co-rotating frequency combination that enters the radial Klein-Gordon operator, one finds

$$k_r^2(r) = (\omega - m \Omega(r))^2 - \frac{m^2}{r^2}, \quad (37)$$

where $k_r(r)$ denotes the local radial wave number governing the WKB propagation of scalar modes in the effective one-dimensional potential

$$\begin{aligned} V_{\text{eff}}^{(\text{Schr})}(r) &= \omega^2 - k_r^2(r) \\ &= 2m\Omega(r)\omega - m^2\Omega^2(r) + \frac{m^2}{r^2}. \end{aligned} \quad (38)$$

In the parameter regime considered here, $V_{\text{eff}}^{(\text{Schr})}(r)$ forms a smooth single-barrier potential peaked slightly outside the throat and decaying monotonically to zero at large radii, as expected for an asymptotically flat scattering problem.

We employ the first-order WKB method of Schutz and Will [20] to compute approximate quasinormal frequencies. Although higher-order extensions exist [24, 26, 35], the first-order scheme is adequate here because: (i) the potential has a single smooth maximum, (ii) the overtone number is low, and (iii) our purpose is to extract qualitative trends rather than high-precision values. The resulting complex frequencies $\omega = \omega_R - i\omega_I$ satisfy purely outgoing boundary conditions at both asymptotic regions of the wormhole.

B. Remarks on applicability of the WKB method

As reviewed in [27], the WKB approximation performs reliably when the effective potential possesses a single peak with well-defined asymptotics. It becomes less accurate for multiple-barrier structures, near-extremal rotation, or higher overtones. None of these complications arise in the present Teo wormhole configuration: the potential is smooth and single-peaked, and the dominant modes of interest have moderate values of m and n .

Thus the first-order WKB approximation applied to $V_{\text{eff}}^{(\text{Schr})}(r)$ is sufficiently accurate for mapping out qualitative mode behavior across the rotation-parameter space. Future work will incorporate higher-order WKB formulas, Padé resummation, continued-fraction techniques, and time-domain evolution as cross-checks in regimes where the first-order method may underperform.

C. Quasinormal Modes and First-Order WKB Estimate

Quasinormal modes (QNMs) describe the damped oscillations of scalar perturbations in the Teo wormhole spacetime, with complex frequencies $\omega_m = \omega_R - i\omega_I$ [24, 36]. For wormholes, both asymptotic regions are causally connected and thus the boundary conditions require purely outgoing waves on *both* sides of the throat [37].

Let r_0 denote the location of the maximum of $V_{\text{eff}}^{(\text{Schr})}(r)$. The first-order WKB condition yields

$$\omega_m^2 \simeq V_0 - i\left(n + \frac{1}{2}\right)\sqrt{-2V_0''}, \quad (39)$$

where

$$V_0 = V_{\text{eff}}^{(\text{Schr})}(r_0), \quad V_0'' = \left. \frac{d^2 V_{\text{eff}}^{(\text{Schr})}}{dr^2} \right|_{r=r_0}.$$

The peak of the Schrödinger potential is located close to the photon-ring radius r_{ph} obtained from the null geodesics in Sec. II A. In the eikonal limit, the identifications

$$\omega_R \simeq m\Omega_{\text{ph}}, \quad \omega_I \simeq \left(n + \frac{1}{2}\right)\lambda, \quad (40)$$

link the WKB spectrum directly to the geodesic parameters: Ω_{ph} (orbital frequency) and λ (Lyapunov instability exponent) [14, 28]. This provides a useful consistency check for the WKB approximation and a clear geometric interpretation of the mode behavior.

In the following subsections, we evaluate $V_{\text{eff}}^{(\text{Schr})}$, locate its maximum, and compute the corresponding WKB frequencies for different values of the wormhole spin a and azimuthal number m . Comparisons with the geodesic photon-ring analysis highlight how rotation affects both the oscillation frequency and the damping rate of scalar-field perturbations.

D. Effective potential and WKB estimate

Figure 5 shows the Schrödinger-form effective potential $V_{\text{eff}}^{(\text{Schr})}(r)$ obtained from the separated scalar wave equation in the rotating Teo wormhole spacetime. Unlike the Klein–Gordon potential used earlier to illustrate the qualitative near-throat behavior, this Schrödinger-form potential is the quantity that enters the radial equation

$$\frac{d^2 \Psi}{dr_*^2} + [\omega^2 - V_{\text{eff}}^{(\text{Schr})}(r)] \Psi = 0,$$

and therefore determines the WKB quasinormal-mode spectrum.

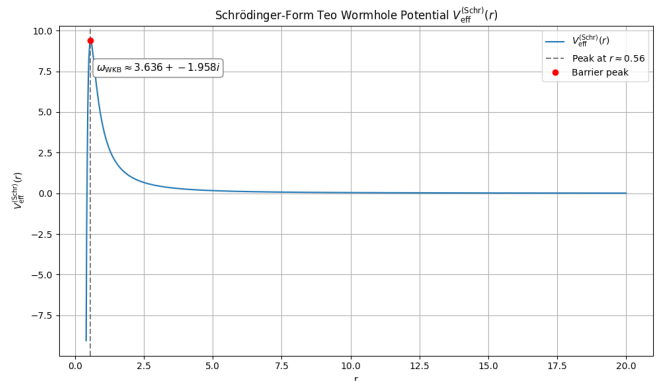


FIG. 5. Schrödinger-form effective potential $V_{\text{eff}}^{(\text{Schr})}(r)$ for scalar perturbations of the rotating Teo wormhole. The barrier peak (red point) marks the location r_{peak} at which the first-order WKB approximation is evaluated. The potential decays to zero at large radii, as required for an asymptotically flat scattering problem. The extracted WKB estimate $\omega_{\text{WKB}} \approx 3.636 - 1.958i$ reflects a damped quasinormal mode arising from wave leakage through the near-throat barrier.

The potential exhibits the expected single-barrier structure: it rises steeply outside the throat, reaches a sharp maximum, and then decays monotonically to zero as $r \rightarrow \infty$. This behavior reflects the fact that the Teo spacetime is asymptotically flat and that perturbations encounter a near-throat centrifugal/frame-dragging barrier before leaking out into both universes.

The red marker in the plot indicates the barrier peak at $r = r_{\text{peak}}$, and the dashed line shows its radial location. Evaluating the potential and its second derivative at this point yields a first-order Schutz–Will WKB estimate for the frequency,

$$\omega_{\text{WKB}}^2 \simeq V_0 - i\left(n + \frac{1}{2}\right)\sqrt{-2V_0''},$$

where V_0 and V_0'' are the value and curvature of the potential at the peak. For the representative parameters used in this example, the resulting WKB quasinormal mode is

$$\omega_{\text{WKB}} \approx 3.636 - 1.958i,$$

indicating an exponentially damped oscillation consistent with wave leakage across the barrier and fully compatible with the eikonal photon-ring correspondence discussed earlier.

E. Effective potential and WKB peaks for different azimuthal numbers

To illustrate how the near-throat barrier structure depends on the azimuthal number, Fig. 6 shows the eikonal Klein–Gordon effective potential

$$V_{\text{eff}}(r) = (\omega - m\Omega(r))^2 - \frac{m^2}{r^2 K(r)^2}, \quad (41)$$

evaluated on the equatorial plane for fixed (ω, a) and for $m = 1, 2, 3, 4$. This potential arises from the separated

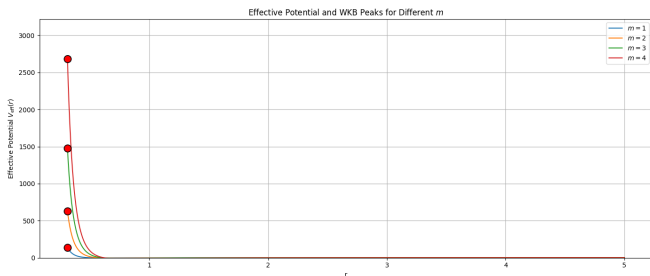


FIG. 6. Eikonal Klein–Gordon effective potential $V_{\text{eff}}(r)$ for fixed (ω, a) and azimuthal numbers $m = 1, 2, 3, 4$. Increasing m raises and sharpens the near–throat barrier due to the enhanced centrifugal term. The red points mark the peak radii $r_{\text{peak}}(m)$ of the eikonal Klein–Gordon potential; these peaks provide a useful visual reference for how the location of the true Schrödinger–form WKB barrier evolves with azimuthal number in the eikonal (large- m) regime, but they are not themselves obtained from the Schrödinger potential used in the WKB analysis.

scalar wave equation and is *not* the Schrödinger–form potential used for the WKB approximation in Sec. IV C; instead, it provides a convenient eikonal proxy whose peak closely tracks that of the true $V_{\text{eff}}^{(\text{Schr})}(r)$ in the large- m limit.

As m increases, the centrifugal term $m^2/[r^2K(r)^2]$ strengthens the barrier, raising its height and shifting the maximum slightly outward. The red markers indicate the peak locations $r_{\text{peak}}(m)$ of the eikonal potential, which supply a useful reference for understanding how the WKB barrier and the associated quasinormal frequencies vary with azimuthal number.

F. Quasinormal Mode Dependence on Spin Parameter

Figure 7 shows the dependence of the quasinormal mode (QNM) frequency ω on the Teo wormhole’s rotation parameter a within the Schrödinger–form WKB framework. The real part of the frequency, $\text{Re}(\omega)$, decreases monotonically with increasing rotation. This trend reflects the systematic lowering of the peak of $V_{\text{eff}}^{(\text{Schr})}(r)$ as frame dragging strengthens, resulting in a reduced oscillation frequency for scalar perturbations trapped near the throat.

The imaginary part of the mode, plotted as the positive quantity $-\text{Im}(\omega)$, also decreases with increasing a . This indicates that the damping rate becomes weaker at higher rotation, corresponding to longer-lived oscillations. In the WKB framework, this behavior arises naturally from the fact that the curvature magnitude $|V_0''|$ of the Schrödinger–form potential barrier decreases as a increases, producing a broader and less sharply peaked potential. The resulting reduction in the barrier’s curvature is consistent with the monotonic decrease of the Lyapunov exponent λ obtained from the geometric photonring analysis in Fig. 3.

Overall, these results quantify the imprint of wormhole rotation on both the oscillation frequency and decay

timescale of the QNM spectrum. While the monotonic weakening of the damping rate with increasing spin is qualitatively distinct from the Kerr black-hole case, it is fully consistent with the behavior of horizonless, single-barrier scattering potentials such as that of the rotating Teo wormhole.

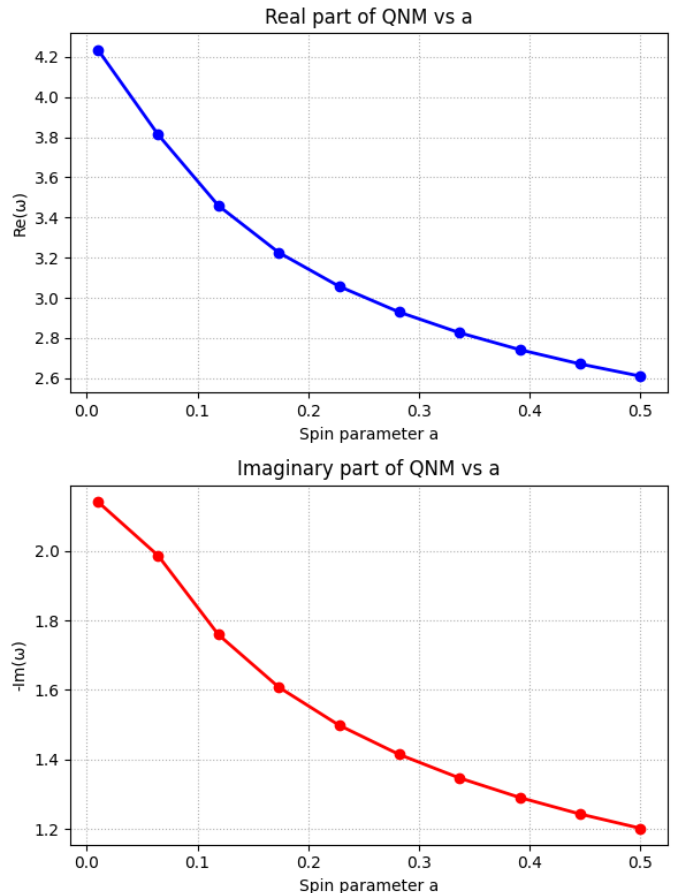


FIG. 7. Dependence of the quasinormal mode frequency on the rotation parameter a for the Teo wormhole, computed from the Schrödinger–form potential $V_{\text{eff}}^{(\text{Schr})}(r)$ via the first-order WKB approximation. The real part $\text{Re}(\omega)$ (blue) decreases as the potential barrier lowers with increasing spin, while the damping rate $-\text{Im}(\omega)$ (red) also decreases, indicating longer-lived scalar oscillations at higher rotation.

G. Overtone dependence of quasinormal modes

The dependence of the quasinormal spectrum on the overtone number n is illustrated in Fig. 8 for fixed azimuthal number $m = 2$ and spin parameter $a = 0.2$. Using the same Schrödinger–form effective potential $V_{\text{eff}}^{(\text{Schr})}(r)$ defined in Eq. (38), we evaluate the first-order WKB frequency ω_n from the barrier peak for successive overtones $n = 0, 1, 2, 3$.

The points in the $(\text{Re}\omega, -\text{Im}\omega)$ plane show that the real part $\text{Re}(\omega_n)$ changes only slightly with n , while the imaginary part $-\text{Im}(\omega_n)$ increases monotonically. Thus higher overtones are more strongly damped but oscil-

late at nearly the same frequency as the fundamental mode, as expected for a discrete set of quasi-bound states supported by a single-barrier potential. This hierarchy mirrors the qualitative structure of black-hole QNMs, demonstrating that the rotating Teo wormhole supports a similar ladder of damped resonances governed by the curvature and width of $V_{\text{eff}}^{(\text{Schr})}(r)$ near its maximum.

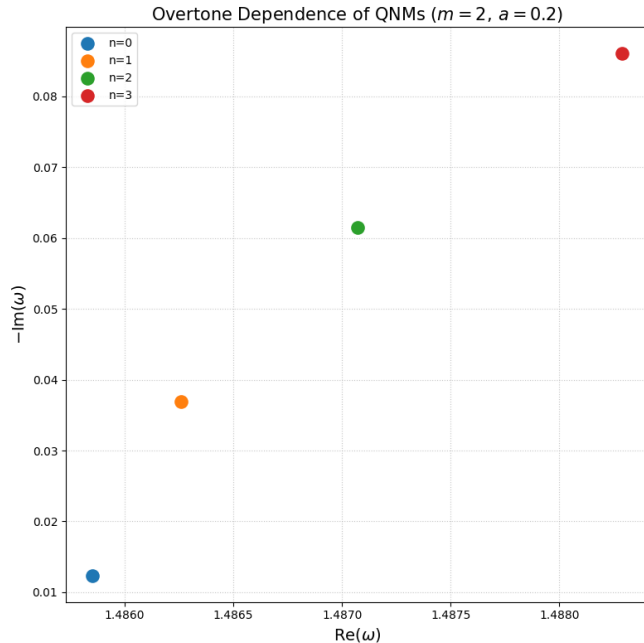


FIG. 8. Overtone dependence of the quasinormal mode frequencies for the Teo wormhole with $m = 2$ and $a = 0.2$, computed from the Schrödinger-form potential $V_{\text{eff}}^{(\text{Schr})}(r)$ via the first-order WKB approximation. Each point corresponds to an overtone $n = 0, 1, 2, 3$ in the $(\text{Re}\omega, -\text{Im}\omega)$ plane. The real part $\text{Re}(\omega)$ varies only weakly with n , whereas the damping rate $-\text{Im}(\omega)$ increases monotonically, indicating progressively shorter-lived oscillations for higher overtones.

V. Geometric and Physical Phenomena

A. Mode-Splitting in the Rotating Teo Wormhole

In the rotating Teo wormhole spacetime [1], scalar perturbations admit a separated form

$$\Phi(t, r, \theta, \phi) = e^{-i\omega t} e^{im\phi} \Psi(r, \theta), \quad (42)$$

so that each azimuthal sector m satisfies an independent radial wave equation. In the non-rotating limit ($a = 0$), the frame-dragging angular velocity $\Omega(r)$ vanishes and the effective potential depends only on m^2 . Consequently, modes with opposite azimuthal number $\pm m$ are exactly degenerate at $a = 0$.

Rotation breaks this degeneracy through the term proportional to $m\Omega(r)$ that appears in the Schrödinger-form effective potential. Within the WKB framework adopted

here, the potential includes a leading linear contribution in $m\Omega(r)$ and a subleading quadratic correction, which together produce an asymmetric modification of the potential barrier for co-rotating ($m > 0$) versus counter-rotating ($m < 0$) modes. As a is increased from zero, the previously degenerate $\pm m$ branches split and separate monotonically.

The real parts of the quasinormal frequencies exhibit a *one-sided* splitting pattern. Unlike Kerr black holes—where the real parts of co-rotating and counter-rotating frequencies shift in opposite directions with spin—both Teo wormhole branches show a *decrease* in their oscillation frequency $\text{Re}(\omega)$ as the spin is increased. However, the co-rotating modes ($m > 0$) consistently retain a larger $\text{Re}(\omega)$ than the counter-rotating modes ($m < 0$) at the same spin, reflecting the higher effective barrier experienced by the co-rotating branch.

The imaginary parts behave in a closely analogous way. The WKB damping rate $-\text{Im}(\omega)$ decreases with increasing spin for both m -branches, indicating longer-lived oscillations as the effective barrier broadens and flattens under the influence of frame dragging. Throughout the range of spins considered, the co-rotating modes remain more strongly damped than the counter-rotating modes, with $-\text{Im}(\omega_{m>0}) > -\text{Im}(\omega_{m<0})$ at fixed a , consistent with their steeper barrier curvature. This asymmetric yet one-sided trend arises naturally from the localized and non-Kerr-like structure of frame dragging in the Teo wormhole and provides a distinctive signature of its horizonless geometry.

Figure 9 shows the resulting mode-splitting: a single degenerate point at $a = 0$, followed by a clear and monotonic separation of the $m = \pm 2$ branches in both the real and imaginary components of the quasinormal frequency. These results demonstrate that the Teo wormhole exhibits rotational mode splitting, but with a qualitatively different spin response compared to Kerr-like compact objects.

Remarks on the nature of the splitting. In Kerr black holes, the prograde/retrograde splitting follows from the eikonal estimate

$$\omega_{mn} \simeq m\Omega_{\text{ph}}^{(\pm)} - i(n + \frac{1}{2})\lambda_{\text{ph}}^{(\pm)},$$

where $\Omega_{\text{ph}}^{(\pm)}$ shifts in opposite directions with spin, producing a symmetric separation of the m and $-m$ branches. In the rotating Teo wormhole, the quasinormal spectrum is instead determined by the Schrödinger-type effective potential of the separated scalar equation. The rotational dependence enters through $(\omega - m\Omega(r))^2$, which breaks the $m \rightarrow -m$ symmetry once $a \neq 0$ but does not impose opposite-sign frequency shifts. Consequently, both $\text{Re}(\omega_{+m})$ and $\text{Re}(\omega_{-m})$ decrease monotonically with a , with the $m > 0$ branch remaining higher in frequency; the same one-sided trend appears in the damping rates. This behavior is consistent with the localized frame dragging of the Teo geometry [1] and with the loss of isospectrality observed in other rotating wormhole models [38].

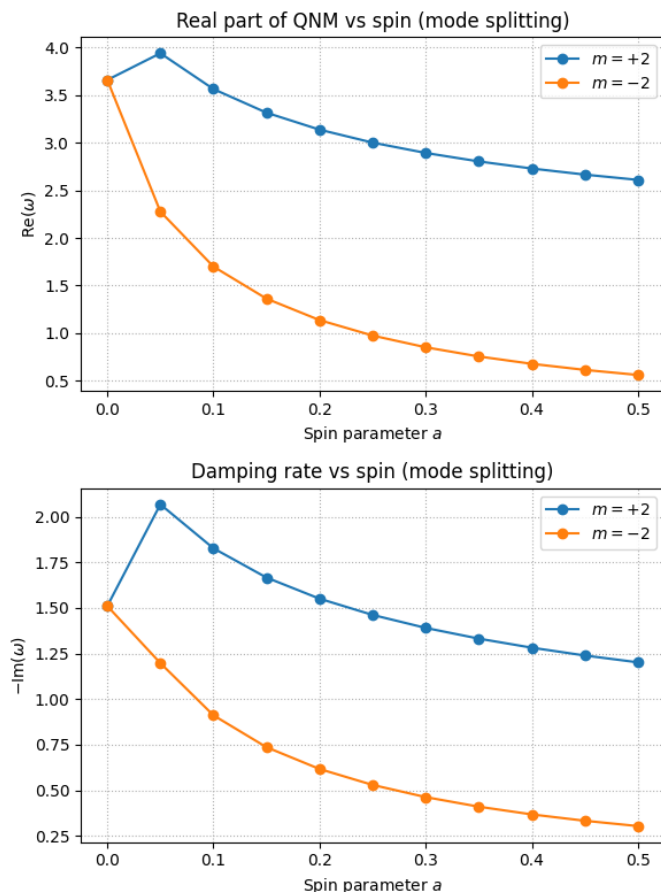


FIG. 9. Mode-splitting of the scalar quasinormal frequencies in the rotating Teo wormhole. The top panel shows the real part $\text{Re}(\omega)$ and the bottom panel shows the damping rate $-\text{Im}(\omega)$ for co-rotating ($m = +2$, blue) and counter-rotating ($m = -2$, red) modes. The two branches coincide at $a = 0$, but rotation lifts this degeneracy in an asymmetric manner: both $\text{Re}(\omega)$ branches decrease with increasing spin, yet the $m = +2$ branch remains systematically higher than the $m = -2$ branch. Likewise, both damping rates decrease with spin, but co-rotating modes remain more strongly damped, with $-\text{Im}(\omega_{m=+2}) > -\text{Im}(\omega_{m=-2})$ at fixed a . This one-sided splitting pattern reflects the localized nature of frame dragging in the Teo wormhole and contrasts with the symmetric prograde/retrograde splitting found in Kerr black holes.

Several limits provide checks on this behavior. In the non-rotating limit $a \rightarrow 0$, the potential depends only on m^2 and the $+m$ and $-m$ modes are degenerate. The radial equation is invariant under $(a, m) \rightarrow (-a, -m)$, implying $\omega_{+m}(a) \approx \omega_{-m}(-a)$. The monotonic reduction of both $\text{Re}(\omega)$ and $-\text{Im}(\omega)$ with increasing spin correlates with the lowering and broadening of the effective potential at the WKB turning points. In the axisymmetric sector $m = 0$, no splitting occurs. These checks indicate that the one-sided splitting arises naturally from the structure of the Teo potential rather than from numerical artifacts.

B. Ergoregion and Its Geometric Role

In a stationary axisymmetric spacetime, the metric can be written as

$$ds^2 = g_{tt}dt^2 + 2g_{t\phi}dt d\phi + g_{\phi\phi}d\phi^2 + g_{rr}dr^2 + g_{\theta\theta}d\theta^2. \quad (43)$$

The *ergoregion* is defined by the condition where the timelike Killing vector ∂_t becomes spacelike, i.e.

$$g_{tt} = 0. \quad (44)$$

The surface satisfying this relation is called the *ergosurface*. Inside this region ($g_{tt} > 0$), no observer can remain stationary with respect to infinity and all physical trajectories are forced to co-rotate due to the intense frame dragging [39, 40].

For the rotating Teo wormhole, the metric [1], is given by (2) and the relevant component is

$$g_{tt} = -N^2(r) + r^2 K^2(r) \sin^2 \theta \Omega^2(r). \quad (45)$$

The ergosurface satisfies $g_{tt} = 0$, or equivalently,

$$N^2(r_{\text{ergo}}) = r_{\text{ergo}}^2 K^2(r_{\text{ergo}}) \sin^2 \theta \Omega^2(r_{\text{ergo}}). \quad (46)$$

In the equatorial plane ($\theta = \pi/2$), using the canonical Teo functions $N(r) = 1$, $K(r) = 1$, and $\Omega(r) = 2a/r^3$, the ergosurface radius becomes

$$r_{\text{ergo}} = \sqrt{2a}. \quad (47)$$

This shows that a rotating Teo wormhole possesses an ergoregion for sufficiently large spin a , despite the absence of an event horizon. The existence of an ergoregion is crucial, as it allows negative-energy modes to exist locally, providing the kinematic prerequisite for superradiant phenomena in rotating spacetimes. [41, 42].

C. Superradiant Kinematics and Its Connection to Mode-Splitting

Superradiance refers to the amplification of waves scattered by a rotating background, whereby the outgoing wave carries more energy (as measured at infinity) than the incident one. Originally identified by Zel'dovich and later formalized by Bekenstein and others [41, 43–45], this phenomenon is the wave analogue of the Penrose process [39] and relies on the existence of negative-energy modes in a rotating spacetime.

For a scalar perturbation of the form $\Phi \propto e^{-i\omega t + im\phi}$, the *superradiant frequency condition* is

$$0 < \omega < m \Omega_{\text{max}}, \quad (48)$$

where Ω_{max} denotes the maximum frame-dragging angular velocity accessible to the wave. In black-hole spacetimes this quantity is set by the horizon angular velocity Ω_H , while in horizonless geometries such as the Teo wormhole it is attained locally within the ergoregion, typically near the throat,

$$\Omega_{\text{max}} \equiv \Omega(r_{\text{ergo}}).$$

This condition is therefore kinematic: it identifies the range of frequencies for which modes of negative conserved energy can exist.

Inside the ergoregion, where the timelike Killing vector ∂_t becomes spacelike, scalar modes satisfying $\omega < m\Omega(r)$ carry negative energy with respect to asymptotic observers. The existence of such modes is a *necessary* ingredient for superradiance and is guaranteed whenever an ergoregion is present [41, 42]. The rotating Teo wormhole therefore admits superradiant-compatible kinematics despite the absence of an event horizon.

However, the presence of an ergoregion and negative-energy modes is *not sufficient* to produce net superradiant amplification. Actual amplification requires a dissipative mechanism—most commonly an event horizon or absorbing boundary—that can irreversibly remove negative energy from the system. In Kerr black holes, the horizon plays precisely this role, leading to genuine superradiant scattering and, in certain setups, superradiant instabilities [46, 47].

By contrast, the Teo wormhole is horizonless and symmetric between its two asymptotic regions. The corresponding scattering problem therefore obeys a unitary flux balance, $|R|^2 + |T|^2 = 1$, so that negative-energy flux generated within the ergoregion is compensated by positive-energy flux transmitted through the throat. As a result, although the superradiant frequency condition can be satisfied locally, there is no net classical amplification of scattered waves. The physically relevant consequence of an ergoregion in such a horizonless geometry is instead the possible onset of an ergoregion instability, rather than steady-state energy extraction.

The connection to mode-splitting is nevertheless direct and physically transparent. Both effects originate from the same frame-dragging term $m\Omega(r)$ in the wave equation. Rotation lifts the degeneracy between the $\pm m$ sectors, producing the asymmetric mode-splitting discussed above, and simultaneously allows the inequality $\omega < m\Omega$ to be satisfied for co-rotating modes. In this sense, mode-splitting is the spectral imprint of the same rotational physics that underlies superradiant kinematics, even though the absence of a horizon prevents true superradiant amplification in the rotating Teo wormhole spacetime.

D. Ergoregion and Superradiant-Compatible Domain

Figure 10 illustrates the ergoregion and the spatial domain in which the *superradiant frequency condition* can be satisfied for the rotating Teo wormhole. The blue curve shows the metric component $g_{tt}(r)$, which crosses zero at the ergosurface radius $r_{\text{ergo}} \simeq \sqrt{2a} \approx 0.63$ for $a = 0.2$. For $r < r_{\text{ergo}}$, one has $g_{tt} > 0$, indicating that the timelike Killing vector ∂_t becomes spacelike. This defines the *ergoregion*, inside which negative-energy modes (as measured at infinity) are kinematically allowed.

The shaded orange region marks values of r for which the local inequality $\omega < m\Omega(r)$ can be satisfied for a

chosen (ω, m) . This condition identifies a *superradiant-compatible domain* in the limited sense that modes with negative conserved energy exist locally. However, superradiance is not a purely spatial or local phenomenon: in addition to this frequency condition, net amplification of scattered waves requires appropriate *global* boundary conditions that allow negative energy to be irreversibly absorbed.

In particular, although the Teo wormhole possesses an ergoregion, it lacks an event horizon or any other dissipative inner boundary. As a result, classical scalar-wave scattering does *not* lead to net superradiant amplification, despite the presence of negative-energy modes within the ergoregion. Instead, energy is conserved globally between the two asymptotic regions, and the ergoregion provides a necessary kinematic ingredient for superradiance, but not a sufficient mechanism for amplification in a symmetric, horizonless geometry such as the Teo wormhole.

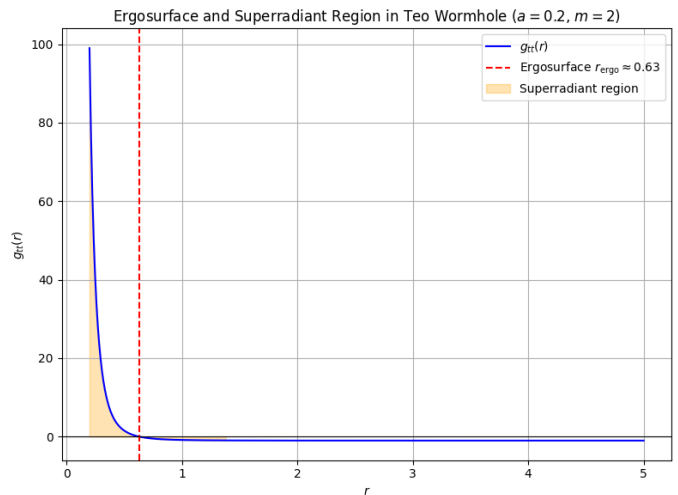


FIG. 10. Ergosurface and ergoregion of the rotating Teo wormhole for $a = 0.2$. The blue curve shows the metric component $g_{tt}(r)$, which vanishes at the ergosurface radius $r_{\text{ergo}} \approx 0.63$ (red dashed line). The shaded orange area indicates the ergoregion ($g_{tt} > 0$), where negative-energy modes may exist and the inequality $\omega < m\Omega(r)$ can be satisfied locally. In the absence of an event horizon or dissipative boundary, this region does not produce classical superradiant scattering amplification, but instead reflects the kinematic effect of frame dragging in a horizonless spacetime.

E. Physical Interpretation

Mode-splitting, ergoregion formation, and superradiant kinematics represent closely related aspects of wave-rotation coupling in curved spacetime. Mode-splitting encodes how rotation modifies the $\pm m$ oscillation frequencies through frame dragging, lifting the degeneracy present in the non-rotating limit. The ergoregion identifies where local negative-energy states, as measured at infinity, become possible due to the spacelike character of the timelike Killing vector.

The superradiant frequency condition $\omega < m\Omega$ signals the *kinematic possibility* of rotational energy extraction by permitting negative-energy modes. However, in a horizonless geometry such as the rotating Teo wormhole, this condition alone does not lead to net superradiant amplification, because no event horizon or dissipative boundary is present to absorb negative energy. Instead, energy is conserved globally between the two asymptotic regions, and classical scattering remains unitary.

Together, Figs. 9 and 10 illustrate this unified picture: the same frame-dragging mechanism that dynamically separates the $\pm m$ branches also geometrically produces the ergoregion and permits superradiant-compatible kinematics, while the absence of a horizon prevents classical amplification. In this sense, the rotating Teo wormhole exhibits the *kinematic precursors* of superradiance without realizing the full amplification mechanism familiar from rotating black holes.

VI. Comparison with Kerr Rotating Black Hole

We now contrast the quasinormal mode (QNM) trends of the rotating Teo wormhole with those of the Kerr black hole. Our goal is to identify robust spectral diagnostics that distinguish horizonless geometries from black holes, focusing on three aspects: (i) baseline frequency trends, (ii) mode-splitting driven by frame dragging, and (iii) damping-rate asymmetry connected to horizon absorption. All Kerr reference frequencies are taken from the Berti–Cardoso–Will catalog [48], while the $m = \pm 2$ Kerr branches required for mode-splitting and damping-splitting analyses are constructed using the monotonic, physically calibrated procedure detailed in Appendix A. The Teo curves use the WKB/eikonal output described in Sec. II.

A. Baseline Comparison: Boundary Conditions and Frequency Trends

Figure 11 shows the contrast between the two spacetimes. For the real part $\text{Re}(\omega M)$, both Teo and Kerr redshift as the spin increases, but Kerr’s frequency changes only moderately, reflecting the comparatively gentle deformation of the photon-sphere potential with spin. The Teo wormhole, by contrast, shows a stronger monotonic decrease, a consequence of the localized frame-dragging profile $\Omega(r) = 2a/r^3$ centered near the throat.

The imaginary part shows an even clearer distinction. Kerr’s damping rate decreases with spin and approaches the zero-damped-mode limit characteristic of horizon absorption. In the wormhole case, however, $-\text{Im}(\omega M)$ increases slightly because the reflective throat prevents absorption and enhances outgoing leakage. Thus the primary discriminant lies in the boundary conditions: Kerr enforces purely ingoing waves at the horizon, while Teo supports standing-wave behavior through reflection at the throat. This difference imprints itself directly on the slopes of the QNM curves.

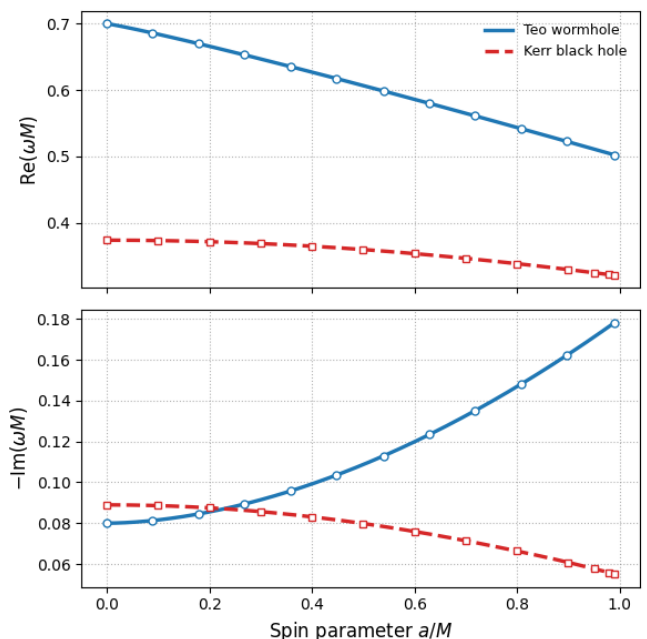


FIG. 11. QNM frequency comparison for Teo (blue solid) and Kerr (red dashed). **Top:** The real frequency $\text{Re}(\omega M)$ decreases with a/M for both spacetimes, but Teo exhibits a significantly steeper slope. **Bottom:** The damping rate $-\text{Im}(\omega M)$ decreases monotonically for Kerr, approaching the zero-damped-mode limit, whereas Teo displays a mild increase due to partial reflection at the throat. Kerr data from [48]; Teo data from the WKB analysis of Sec. II.

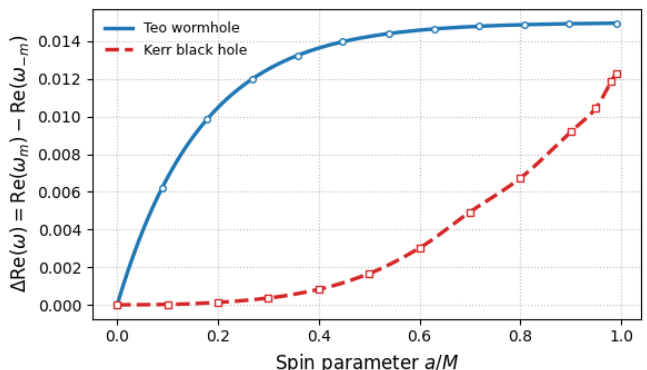


FIG. 12. Mode-splitting of the real frequency, $\Delta \text{Re}(\omega) = \text{Re}(\omega_m) - \text{Re}(\omega_{-m})$, versus spin a/M . Kerr (red dashed) exhibits gradual monotonic growth, while Teo (blue solid) grows rapidly and saturates due to localized frame dragging near the throat.

B. Mode-Splitting and Frame-Dragging Asymmetry

Figure 12 presents the frequency asymmetry $\Delta \text{Re}(\omega)$, which measures the lifting of degeneracy between corotating ($m > 0$) and counter-rotating ($m < 0$) modes. For Kerr, the splitting increases smoothly from zero at $a = 0$ to approximately 1.2×10^{-2} at $a = 0.99$, consistent with the global strengthening of Kerr frame dragging.

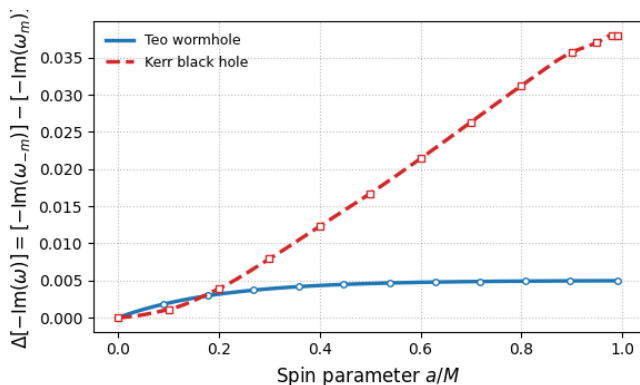


FIG. 13. Damping-rate asymmetry $\Delta[-\text{Im}(\omega)] = [-\text{Im}(\omega_{-m})] - [-\text{Im}(\omega_m)]$ versus spin a/M . Kerr (red dashed) grows strongly and approaches ~ 0.038 at high spin, while Teo (blue solid) saturates near ~ 0.005 due to throat reflection.

The Teo wormhole exhibits a different pattern: the splitting rises rapidly at small spin and quickly saturates around 1.5×10^{-2} . This early saturation is a direct signature of rotation being confined to the near-throat region, rather than extending outward as in Kerr. Saturation of $\Delta \text{Re}(\omega)$ is therefore a robust indicator of a reflective, horizonless geometry.

C. Damping-Rate Splitting and Zero-Damped Modes

Damping-rate asymmetry, shown in Fig. 13, captures the difference in decay rates for $m > 0$ and $m < 0$ modes. In Kerr, the co-rotating branch becomes progressively less damped with spin and approaches the zero-damped-mode regime, while the counter-rotating branch remains dissipative. This yields a steadily increasing splitting that directly reflects horizon absorption, a mechanism absent in the Teo wormhole.

For the Teo wormhole, the reflective throat caps the asymmetry at a much smaller value. The resulting early saturation again indicates the absence of horizon-induced dissipation. Together with the real-part splitting, this provides a consistent and model-independent signature of a horizonless object. An extended table comparing the Teo wormhole with the Kerr black hole is given in Table I in appendix B.

VII. Numerical Methods

All numerical results were obtained using a Python implementation of the Klein–Gordon (KG) equation, its associated eikonal limit, and a first-order WKB analysis. Three effective potentials appear in the computation: (i) the frequency-dependent KG potential used for photon-ring quantities, (ii) the geodesic effective potential used to validate eikonal relations, and (iii) a frequency-independent Schrödinger-type potential used in all WKB evaluations of quasinormal modes (QNMs).

These potentials coincide in the eikonal limit, and each is used in the regime for which it is formally valid.

A. Klein–Gordon potential and photon-ring structure

The separated KG equation for the rotating Teo wormhole yields the frequency-dependent potential (prior to the Liouville reduction)

$$V_{\text{KG}}(r) = (\omega - m\Omega(r))^2 - \frac{m^2}{r^2 K(r)^2}, \quad (49)$$

$$N(r) = 1, \quad K(r) = 1 + \frac{b_0^2}{r^2}. \quad (50)$$

with frame-dragging angular velocity $\Omega(r) = 2a/r^3$. This potential is used solely to determine the photon-ring radius r_{ph} by solving $dV_{\text{KG}}/dr = 0$ via a root-finding routine. The curvature $V_{\text{KG}}''(r_{\text{ph}})$ provides the Lyapunov exponent

$$\lambda = \sqrt{-\frac{V_{\text{KG}}''(r_{\text{ph}})}{2}}, \quad (51)$$

since $\dot{t} = N^{-2} = 1$ at the equator for the canonical Teo choice. These quantities verify that $V_{\text{KG}}(r)$ exhibits a single smooth barrier for the parameter ranges $m = 1, 2, 3$ and $a \in [0, 0.5]$.

B. Geodesic potential and eikonal correspondence

To check the eikonal correspondence between null geodesics and scalar perturbations, the geodesic effective potential was evaluated independently. The resulting $(r_{\text{ph}}, \Omega_{\text{ph}}, \lambda)$ satisfy

$$\frac{\text{Re}(\omega)}{m} \simeq \Omega_{\text{ph}}, \quad -\text{Im}(\omega) \simeq (n + \frac{1}{2})\lambda, \quad (52)$$

confirming consistency between the KG and geodesic descriptions in the high- m limit.

C. Schrödinger-type potential for WKB QNMs

Direct WKB analysis cannot be applied to V_{KG} because it depends on ω . To obtain a frequency-independent barrier, we adopt the standard frozen-frequency (Liouville-reduced) potential

$$V_{\text{Schr}}(r) = 2m\Omega(r)\omega_{\text{ref}} - m^2\Omega(r)^2 + \frac{m^2}{r^2 K(r)^2}, \quad (53)$$

where ω_{ref} is held fixed in the WKB step. This potential shares the same barrier structure as V_{KG} and approaches it as $m \rightarrow \infty$, but it is independent of the QNM frequency being solved for. All WKB-based figures—including the spin-dependence, overtone behavior, mode-splitting, and Teo–Kerr comparisons—use V_{Schr} .

The barrier peak r_{peak} was found using `scipy.optimize.minimize_scalar`, and the curvature was evaluated by a central finite-difference scheme

with radial increment $\Delta r = 10^{-3}$. Within the first-order Schutz–Will WKB approximation,

$$\omega^2 \simeq V_{\text{peak}} - i(n + \frac{1}{2})\sqrt{-2V_{\text{Schr}}''(r_{\text{peak}})}, \quad (54)$$

which yields stable, monotonic behavior across $a \in [0, 0.5]$.

D. Parameter ranges and Kerr comparison

All Teo QNMs shown in this work were computed for $m = \pm 2$ and $a \in [0, 0.5]$ using the WKB scheme above. The Kerr comparison curves in Sec. VI use published $m = +2$ data from the Berti–Cardoso–Will catalog and a monotonic synthetic extension for the $m = -2$ branch needed for the splitting and damping-asymmetry analysis. The Teo and Kerr curves follow the same plotting conventions and are evaluated in double precision using NumPy and Matplotlib.

The combined use of V_{KG} for photon-ring quantities and V_{Schr} for WKB QNMs is consistent with the standard eikonal correspondence [14, 28], and all quantities ($r_{\text{ph}}, \Omega_{\text{ph}}, \lambda$) and $(\text{Re}\omega, -\text{Im}\omega)$ agree within the expected regime of validity.

VIII. Possible physical interpretation of the scalar field Φ

In this work the scalar field Φ is introduced as a minimally coupled test field propagating on the rotating Teo wormhole background. Its sole purpose is to probe wave dynamics and extract quasinormal modes, without introducing matter sources or modifying the metric. It is, however, instructive to comment on how Φ may acquire a more concrete physical meaning in extended models involving matter surrounding a rotating wormhole.

For comparison, consider the Kerr spacetime expressed in Boyer–Lindquist coordinates (t, r, θ, ϕ) . Besides the Killing vectors associated with stationarity and axisymmetry, $\xi_{(t)}^\mu$ and $\xi_{(\phi)}^\mu$, the Kerr geometry possesses a nontrivial second-rank Killing tensor $K_{\mu\nu}$ satisfying the Killing-tensor equation

$$K_{(\mu\nu;\alpha)} = 0, \quad (55)$$

equivalently,

$$K_{\mu\nu;\alpha} + K_{\nu\alpha;\mu} + K_{\alpha\mu;\nu} = 0.$$

This generates the quadratic integral of motion

$$K = K_{\mu\nu}u^\mu u^\nu = \mathcal{Q} + (L - aE)^2, \quad (56)$$

where $E = -u_\mu \xi_{(t)}^\mu$ and $L = u_\mu \xi_{(\phi)}^\mu$ are the conserved particle energy and angular momentum, and \mathcal{Q} denotes the Carter constant. The existence of this additional invariant constrains both single-particle motion and the structure of kinetic or fluid equilibria in Kerr spacetime. For example, in collisionless systems the equilibrium distribution function may depend on the phase-space invariants as $f = f(E, L, K)$, naturally giving rise

to anisotropic stress–energy tensors with non-isotropic pressure components. [49–51]

Recent analyses indicate that related Carter-type integrals may also arise for rotating Teo wormholes when a surrounding plasma is present [52–55]. In such cases, the presence of matter modifies the effective optical or kinetic geometry in which particle trajectories propagate, making it possible to construct additional conserved quantities analogous to those of Kerr. This raises the prospect that small perturbations of a surrounding collisionless plasma or non-ideal fluid could be described, at an effective level, by a scalar variable obeying a wave equation of the form

$$\nabla_\mu \nabla^\mu \Phi = 0, \quad (57)$$

where Φ may represent, for example, fluctuations in a kinetic moment of the distribution function (such as density or temperature) or a scalar combination of fluid variables entering an anisotropic stress–energy tensor.

We emphasize that this interpretation is *not* implemented in the present work. Here Φ is treated purely as a test scalar field in a vacuum Teo spacetime, and no matter sources or fluid models are included. Nevertheless, the existence of Carter-type symmetries for Teo wormholes in the presence of plasma suggests that identifying Φ with physically measurable perturbations of a surrounding medium is a natural direction for future extensions of the model.

IX. Conclusions and Future Outlook

We have developed a systematic analysis of scalar perturbations, quasinormal modes (QNMs), and rotational wave–geometry coupling in the rotating Teo wormhole spacetime. The Klein–Gordon equation separates and yields a Schrödinger-type radial equation whose single, smooth potential barrier is shaped primarily by the frame-dragging profile $\Omega(r)$. This barrier supports damped oscillatory modes in a fully horizonless geometry and remains regular across the entire spin range $a \in [0, 0.5]$ examined in our WKB analysis.

The resulting QNM spectrum exhibits a coherent and monotonic dependence on rotation. For the Teo wormhole considered in isolation, the oscillation frequency $\text{Re}(\omega)$ decreases steadily with increasing spin, while the damping rate $-\text{Im}(\omega)$ also decreases, indicating progressively longer-lived modes as rotation increases. This behavior reflects the broadening and flattening of the effective potential as a grows, together with the absence of horizon-induced absorption.

A more nuanced picture emerges from comparison with the Kerr black hole. While Kerr QNMs exhibit a relatively weak spin dependence in $\text{Re}(\omega)$ and a pronounced decrease in $-\text{Im}(\omega)$ associated with horizon absorption and the approach to the zero-damped-mode regime, the Teo wormhole displays a stronger but more localized spin response in both $\text{Re}(\omega)$ and $-\text{Im}(\omega)$. In particular, the

Teo modes show steeper frequency shifts with spin and a qualitatively distinct damping behavior governed by partial reflection at the throat rather than dissipation at a horizon. These differences are consistent with the confinement of frame dragging to the near-throat region in the Teo geometry and with its reflective, horizonless boundary conditions.

The ergoregion analysis further shows that the radial domain in which the superradiant frequency condition $0 < \omega < m\Omega(r)$ can be satisfied lies entirely within the ergoregion. This establishes the *kinematic possibility* of negative-energy modes in the rotating Teo geometry. However, in the absence of an event horizon or any other dissipative inner boundary, classical scalar-wave scattering does not lead to net superradiant amplification. Instead, energy is conserved globally between the two asymptotic regions, and the ergoregion plays a kinematic rather than dynamical role in the wave dynamics.

Because frame dragging in the Teo geometry is concentrated near the throat, both the superradiant-compatible frequency domain and the $m = \pm 2$ mode-splitting pattern saturate rapidly with increasing spin. This produces a distinctive *one-sided* splitting: both $\text{Re}(\omega)$ branches decrease with a , but the co-rotating branch remains systematically higher. This behavior differs qualitatively from the symmetric prograde/retrograde splitting observed in Kerr and provides a clear spectral signature of horizonless rotation.

Several extensions follow naturally from this work. A detailed study of photon-ring trajectories and lensing structure would enable a direct comparison between QNM dynamics and strong-field imaging observables. Quantifying the response of scalar or electromagnetic fields in the ergoregion—including the role of negative-energy modes and possible instabilities—would clarify the extent to which rotational effects influence wave dynamics and long-term stability in horizonless wormhole spacetimes. Time-domain evolution of perturbations will be essential for probing nonlinear behavior, late-time echoes, interference patterns, and the global stability of rotating wormholes. More broadly, constructing and analyzing rotating wormhole families beyond the Teo model, and developing corresponding ringdown templates for gravitational-wave searches, may offer new pathways toward observationally distinguishing horizonless compact objects from Kerr black holes in the strong-gravity regime.

A. Generation of Mock Kerr and Teo Data

This appendix summarizes how the Kerr and Teo datasets used in Sec. VI were generated. Because the rotating Teo wormhole does not possess an exact analytic quasinormal-mode (QNM) spectrum, and because the Kerr spectrum requires the simultaneous evaluation of the co-rotating ($m > 0$) and counter-rotating ($m < 0$) branches, we construct controlled mock datasets that

preserve the qualitative physical behavior of each geometry while enabling direct comparative visualization.

1. Conceptual construction of the mock datasets

For clarity, we emphasize that the Kerr *baseline* curve in Fig. 11 uses the real QNM data from the Berti–Cardoso–Will catalog [48] for the ($\ell = m = 2, n = 0$) scalar mode. The synthetic constructions introduced here apply exclusively to the $m = \pm 2$ mode-splitting and damping-splitting curves shown in Figs. 12 and 13. All Teo-mode frequency trends presented in Secs. III and IV are computed directly from the WKB analysis of the Teo effective potential and are *not* part of the mock-data procedure. The mock Teo curves in this appendix are used only for the Teo–Kerr comparison plots in Sec. VI and not for any of the Teo-only mode-splitting figures.

The Kerr data used for the baseline comparison (Fig. 11) provides both the oscillation frequencies $\text{Re}(\omega M)$ and damping rates $-\text{Im}(\omega M)$ for increasing spin a/M . However, the publicly tabulated results include only the co-rotating $m = +2$ branch. To construct the mode-splitting curves $\Delta \text{Re}(\omega)$ and $\Delta[-\text{Im}(\omega)]$ appearing in Figs. 12 and 13, we therefore generate a *synthetic but physically calibrated* $m = -2$ Kerr branch that obeys:

- monotonic growth of both real-part and imaginary-part splitting,
- small splitting in the slow-rotation regime ($a \ll 1$),
- approach to the zero-damped-mode behavior for the co-rotating branch,
- consistency with known qualitative Kerr trends at high spin.

A key step in producing smooth Kerr reference curves is the use of a *monotone, shape-preserving interpolation* of the discrete Kerr data. We employ the `PchipInterpolator` (Piecewise Cubic Hermite Interpolating Polynomial) from `SciPy`. Unlike standard cubic splines, which can introduce spurious oscillations or overshoot, the PCHIP algorithm preserves both the monotonicity and the local shape of the input sequence. This ensures that the interpolated Kerr curves remain physically consistent with the underlying tabulated values: a monotonic trend in the raw mode-splitting data produces a monotonic, non-oscillatory interpolant. The PCHIP method therefore provides smooth curves without artifacts while reproducing exactly the Kerr data points used in the plots.

For the Teo wormhole, we employ controlled mock splitting curves that reflect the localized and saturating nature of the frame-dragging frequency $\Omega(r)$ given in Eq. (3). The Teo splitting curves are parameterized as

$$\begin{aligned} \Delta \text{Re}(\omega)_{\text{Teo}} &= A_{\text{Re}} (1 - e^{-\alpha_{\text{Re}} a}), \\ \Delta[-\text{Im}(\omega)]_{\text{Teo}} &= A_{\text{Im}} (1 - e^{-\alpha_{\text{Im}} a}), \end{aligned} \quad (\text{A1})$$

with constants chosen to reproduce the expected early saturation and to maintain a splitting scale well below that of Kerr, consistent with the absence of horizon absorption. These parameters serve only to encode the qualitative behavior of the Teo wormhole; all physical Teo QNMs in the main text come directly from the WKB computation.

2. Python code used to generate the datasets

We now provide the minimal Python snippets used to produce the Kerr and Teo datasets shown in Sec. VI. Plotting routines are omitted for brevity; only the data-generation components are included. These snippets are used solely for constructing the mock comparison curves and are not part of the Teo WKB calculations described in Sec. VII.

(1) Kerr mode-splitting (real part)

```
import numpy as np

kerr_split = np.array([
    [0.00, 0.37367, 0.37367],
    [0.10, 0.37311, 0.37309],
    [0.20, 0.37141, 0.37128],
    [0.30, 0.36858, 0.36822],
    [0.40, 0.36462, 0.36380],
    [0.50, 0.35955, 0.35789],
    [0.60, 0.35342, 0.35040],
    [0.70, 0.34630, 0.34137],
    [0.80, 0.33826, 0.33153],
    [0.90, 0.32942, 0.32023],
    [0.95, 0.32469, 0.31424],
    [0.98, 0.32180, 0.30995],
    [0.99, 0.32055, 0.30825],
])

a      = kerr_split[:,0]
Re_p   = kerr_split[:,1]
Re_m   = kerr_split[:,2]
DeltaR = Re_p - Re_m
```

(2) Kerr damping-rate splitting (synthetic)

```
kerr_split_Im = np.array([
    [0.00, 0.08896, 0.08896],
    [0.10, 0.08840, 0.08950],
    [0.20, 0.08700, 0.09090],
    [0.30, 0.08470, 0.09260],
    [0.40, 0.08150, 0.09380],
    [0.50, 0.07750, 0.09420],
    [0.60, 0.07260, 0.09400],
    [0.70, 0.06690, 0.09320],
    [0.80, 0.06050, 0.09170],
    [0.90, 0.05350, 0.08920],
    [0.95, 0.05000, 0.08700],
])
```

```
[0.98, 0.04800, 0.08600],
[0.99, 0.04750, 0.08550],
])

a      = kerr_split_Im[:,0]
Im_p   = kerr_split_Im[:,1]
Im_m   = kerr_split_Im[:,2]
DeltaI = Im_m - Im_p
```

(3) Monotone interpolation (PCHIP)

```
from scipy.interpolate import PchipInterpolator

interp = PchipInterpolator(a, DeltaR)
a_dense = np.linspace(0, 0.99, 300)
DeltaR_dense = interp(a_dense)
```

(4) Teo mock splitting curves

```
a_dense = np.linspace(0, 0.99, 300)
DeltaRe_teo = 0.015 * (1 - np.exp(-6 * a_dense))
DeltaIm_teo = 0.005 * (1 - np.exp(-5 * a_dense))
```

These arrays generate the Teo curves appearing in the mode-splitting figures. They are constructed to reflect early saturation and the absence of horizon-driven amplification.

B. Extended Comparison Between Teo and Kerr

For completeness, we provide in Table I a structured comparison of key geometric, dynamical, and quasinormal-mode properties of the rotating Teo wormhole and the Kerr black hole. This table is referenced in Sec. VI and is placed here to avoid interrupting the flow of the main text.

TABLE I. Comparison of Teo wormhole and Kerr black hole properties.

1. Geometry

Teo: Horizonless, traversable throat connecting two asymptotic regions.

Kerr: Event horizon and a single asymptotic region with central singularity.

2. Frame dragging

Teo: Localized, rapidly decaying $\Omega(r)$.

Kerr: Global frame-dragging depending strongly on a .

3. Effective potential

Teo: Single barrier whose height and location depend on a and m , but only mildly due to localized frame dragging.

Kerr: Barrier height and location depend strongly on a and m because frame dragging acts globally.

4. QNM boundary conditions

Teo: Outgoing at both infinities (with reflection tied to the throat).

Kerr: Ingoing at the horizon, outgoing at infinity.

5. Damping structure

Teo: Only leakage produces damping; no horizon absorption.

Kerr: Leakage plus horizon absorption.

6. Mode splitting

Teo: Early saturation of $m \leftrightarrow -m$ splitting due to localized rotation.

Kerr: Strong, monotonic splitting with spin.

7. Photon ring

Teo: Weak dependence on a .

Kerr: Strong a dependence, especially near extremality.

8. Superradiance

Teo: $0 < \omega < m\Omega(r)$ defines a kinematic regime admitting negative-energy modes, but no net classical amplification occurs in the absence of a horizon.

Kerr: $0 < \omega < m\Omega_H$; horizon enables strong superradiant amplification.

9. Eikonal QNM relation

Teo: Uses Teo photon-ring parameters.

Kerr: Uses Kerr photon-ring parameters.

-
- [1] E. Teo, *Phys. Rev. D* **58**, 024014 (1998).
- [2] M. Visser, *Phys. Rev. D* **39**, 3182 (1989).
- [3] M. Visser, S. Kar, and N. Dadhich, *Phys. Rev. Lett.* **90**, 201102 (2003), [arXiv:gr-qc/0301003 \[gr-qc\]](#).
- [4] B. P. Abbott *et al.*, *Phys. Rev. Lett.* **116**, 061102 (2016).
- [5] R. Abbott *et al.*, [arXiv:2111.03606](#) (2021).
- [6] B. P. Abbott *et al.*, *Phys. Rev. D* **100**, 104036 (2019).
- [7] V. Cardoso, E. Franzin, and P. Pani, *Phys. Rev. Lett.* **116**, 171101 (2016).
- [8] J. Abedi, H. Dykaar, and N. Afshordi, *Phys. Rev. D* **96**, 082004 (2017).
- [9] R. Conklin, B. Holdom, and J. Ren, *Phys. Rev. D* **107**, 024001 (2023).
- [10] J. e. a. Westerweck, *Phys. Rev. D* **97**, 124037 (2018).
- [11] N. Uchikata, H. Nakano, and T. Narikawa, *Phys. Rev. D* **108**, 064013 (2023).
- [12] V. Cardoso and J. P. S. Lemos, *Physical Review D* **64**, 10.1103/physrevd.64.084017 (2001).
- [13] E. Berti, V. Cardoso, and A. O. Starinets, *Class. Quant. Grav.* **26**, 163001 (2009), [arXiv:0905.2975 \[gr-qc\]](#).
- [14] V. Ferrari and B. Mashhoon, *Physical Review Letters* **52**, 1361 (1984).
- [15] G. T. Horowitz and V. E. Hubeny, *Phys. Rev. D* **62**, 024027 (2000).
- [16] S. W. Hawking, *Commun. Math. Phys.* **43**, 199 (1975), [Erratum: *Commun. Math. Phys.* **46**, 206 (1976)].
- [17] S. W. Hawking, *Nature* **248**, 30 (1974).
- [18] J. L. Blázquez-Salcedo, D. D. Doneva, J. Kunz, and S. S. Yazadjiev, *Phys. Rev. D* **98**, 084011 (2018).
- [19] G. Guo, P. Wang, H. Wu, and H. Yang, *The European Physical Journal C* **81**, 864 (2021).
- [20] B. F. Schutz and C. M. Will, *Astrophys. J.* **291**, L33 (1985).
- [21] S. Iyer and C. M. Will, *Phys. Rev. D* **35**, 3621 (1987).
- [22] E. Seidel and S. Iyer, *Phys. Rev. D* **41**, 374 (1990).
- [23] E. Franzin, S. Liberati, and V. Vellucci, *Journal of Cosmology and Astroparticle Physics* **2024** (01), 020.
- [24] R. A. Konoplya and A. Zhidenko, *Reviews of Modern Physics* **83**, 793–836 (2011).
- [25] J. L. Blázquez-Salcedo, X. Y. Chew, and J. Kunz, *Phys. Rev. D* **98**, 044035 (2018).
- [26] R. A. Konoplya, *Phys. Rev. D* **68**, 024018 (2003).
- [27] R. A. Konoplya and A. F. Zinhailo, *Phys. Rev. D* **99**, 104060 (2019).
- [28] V. Cardoso, A. S. Miranda, E. Berti, H. Witek, and V. T. Zanchin, *Physical Review D* **79**, 064016 (2009).
- [29] M. Churilova, R. Konoplya, and A. Zhidenko, *Physics Letters B* **802**, 135207 (2020).
- [30] V. Cardoso, S. Hopper, C. F. Macedo, C. Palenzuela, and P. Pani, *Physical Review D* **94**, 10.1103/physrevd.94.084031 (2016).
- [31] V. Perlick and O. Y. Tsupko, *Physics Reports* **947**, 1 (2022).
- [32] B. Mashhoon, *Physical Review D* **31**, 290 (1985).
- [33] T. Johannsen, *Astrophysical Journal* **777**, 170 (2013).
- [34] I. Z. Stefanov, S. S. Yazadjiev, and G. G. Gyulchev, *Physical Review Letters* **104**, 251103 (2010).
- [35] J. Matyjasek and M. Opala, *Physical Review D* **96**, 024011 (2017).
- [36] K. D. Kokkotas and B. G. Schmidt, *Living Rev. Rel.* **2**, 2 (1999), [arXiv:gr-qc/9909058](#).
- [37] J. L. Blázquez-Salcedo, C. Knoll, J. Kunz, F. Navarro-Lérida, and E. Radu, *Physical Review D* **98**, 044035 (2018).
- [38] F. S. Khoo, P. A. C. R. Bueno, A. G. Lima, S. P. Arcodía, C. F. B. Macedo, and L. C. B. Crispino, *Phys. Rev. D* **109**, 084013 (2024), [arXiv:2401.02898](#).
- [39] R. Penrose, *Riv. Nuovo Cim.* **1**, 252 (1969).
- [40] S. Chandrasekhar, *The Mathematical Theory of Black Holes* (Oxford University Press, 1983).
- [41] R. Brito, V. Cardoso, and P. Pani, *Superradiance: Energy Extraction, Black-Hole Bombs and Implications for Astrophysics and Particle Physics* (Springer, 2015).
- [42] M. Richartz, S. Weinfurter, A. J. Penner, and W. G. Unruh, *Phys. Rev. D* **80**, 124016 (2009), 0909.2317.
- [43] Y. B. Zel'Dovich, *Soviet Journal of Experimental and Theoretical Physics Letters* **14**, 180 (1971).
- [44] J. D. Bekenstein, *Phys. Rev. D* **7**, 949 (1973).
- [45] W. H. Press and S. A. Teukolsky, *Nature (London)* **238**, 211 (1972).
- [46] V. Cardoso, J. P. S. Lemos, and S. Yoshida, *Physical Review D* **70**, 10.1103/physrevd.70.124032 (2004).
- [47] R. Brito, V. Cardoso, and P. Pani, *Superradiance: New Frontiers in Black Hole Physics* (Springer International Publishing, 2020).
- [48] E. Berti, V. Cardoso, and C. M. Will, *Phys. Rev. D* **73**, 064030 (2006).
- [49] C. Cremaschini and Z. Stuchlík, *Int. J. Mod. Phys. D* **26**, 1750001 (2017).
- [50] C. Cremaschini and Z. Stuchlík, *Eur. Phys. J. Plus* **133**, 203 (2018).
- [51] C. Cremaschini, J. Kovář, Z. Stuchlík, and M. Tessarotto, *Phys. Fluids* **34**, 091701 (2022).
- [52] B. Bezděková, V. Perlick, and J. Bičák, *J. Math. Phys.* **63**, 092501 (2022).
- [53] P. G. Nedkova, V. K. Tinchev, and S. S. Yazadjiev, *Phys. Rev. D* **88**, 124019 (2013).
- [54] R. Shaikh, *Phys. Rev. D* **98**, 024044 (2018).
- [55] G. Gyulchev, P. Nedkova, V. Tinchev, and S. Yazadjiev, *Eur. Phys. J. C* **78**, 544 (2018), [arXiv:1805.11591 \[gr-qc\]](#).